An inversion algorithm using neural networks to retrieve atmospheric CO total columns from high-resolution nadir radiances

Juliette Hadji-Lazaro, Cathy Clerbaux, Sylvie Thiria

JOURNAL OF GEOPHYSICAL RESEARCH, VOL. 104, NO. D19, PAGES 23,841–23,854, OCTOBER 20, 1999

An inversion algorithm using neural networks to retrieve atmospheric CO total columns from high-resolution nadir radiances

Juliette Hadji-Lazaro and Cathy Clerbaux

Service d'Aéronomie du CNRS, Institut Pierre-Simon Laplace, Paris

Sylvie Thiria

Laboratoire d'Océanographie Dynamique et de Climatologie, Institut Pierre-Simon Laplace, Paris

Abstract. Up to the first years of the next millennium, several observation programs of the troposphere are scheduled, including the Infrared Atmospheric Sounding Interferometer, which uses Fourier transform spectroscopy to record the radiance of the Earth-atmosphere system with a nadir-viewing geometry. The Interferometric Monitor for Greenhouse Gases (IMG), launched aboard the Advanced Earth Observing System in August 1996, was a precursor of these forthcoming missions. A new inversion algorithm based on neural network techniques is in development to retrieve trace gases from high-resolution nadir radiances. Neural networks offer a technical alternative to classical methods and allow efficient inversion calculations as required to treat the huge volume of data which will be provided by continuous observation of the atmosphere from space. To develop a network to retrieve the carbon monoxide total column, realistic simulations of the IMG measurements were obtained by coupling a three-dimensional chemical-transport model with a high-resolution line-by-line radiative transfer code adjusted to the instrumental features. The application of the algorithm on simulated data allowed the checking of its performance: for about 99% of the cases, the relative inversion error was less than 10%. This algorithm has been applied to the spectra recorded by the IMG instrument between June 16 and 19, 1997. Global-scale distributions of CO total columns were obtained for the first time by using a neural network, and this technique proved its ability to achieve real-time inversion of atmospheric CO.

1. Introduction

Carbon monoxide (CO) is important in tropospheric chemistry. CO affects the concentrations and distributions of the atmospheric oxidants: hydroxyl radical (OH), hydroperoxyl radical (HO_2), and ozone (O_3) [*Novelli et al.*, 1998]. CO is directly removed by the oxidation cycles initiated by chemical reactions with OH, and it is produced by oxidation of methane (CH_4) and nonmethane hydrocarbons (NMHC). As about 75% of the OH radicals react with about 90% of CO [*Logan et al.*, 1981; *Crutzen and Zimmermann*, 1991], these oxidation reactions are the main sinks for CO and OH. Depending on nitrogen oxide ($[NO_x] = [NO] + [NO_2]$) concentrations, the oxidation cycles of CO, CH_4, and NMHC either produce or destroy O_3 in the troposphere. If the NO_x abundance is sufficient (the threshold is not fixed and depends on concentrations of other atmospheric constituents), the hydroperoxyl radical (HO_2), which is produced in the oxidation cycles of CO, CH_4, and NMHC, reacts preferably with NO to form O_3. If the NO_x level is low, HO_2 destroy O_3 [*Novelli et al.*, 1998]. Therefore it appears clearly that CO has an important influence on the oxidizing capacity of the atmosphere.

If the nature of the CO sources and sinks is well known, it remains difficult to quantify their magnitudes. The primary sources of CO are emissions from technological sources, biomass burning, biogenic sources, and oceans, where the technological sources include transportation, combustion, industrial processes, and refuse incinerations. Estimated strengths for the technological sources range from 300 to 900 Tg yr^{-1} and the contribution of biomass burning is estimated to be between 400 and 700 Tg yr^{-1} [*World Meteorological Organization (WMO)*, 1995]. The biogenic sources (vegetation, soils, and animals) and the emissions from oceans con-

Paper number 1999JD900431.
0148-0227/99/1999JD900431$09.00

tribute with lower strengths. The secondary sources of CO are the oxidation of CH_4 and NMHC. These reactions produce between 400 and 1000 Tg yr^{-1} and between 300 and 1300 Tg yr^{-1} of CO, respectively [*WMO,* 1995]. The main sink of CO is the oxidation by OH which removes from 1400 to 2600 Tg yr^{-1} of CO [*WMO,* 1995]. The remaining losses are distributed between soil uptake and transport to the stratosphere with weaker strengths. All these estimates have large uncertainties. To improve the knowledge of the CO spatial and temporal distributions, it is necessary to measure its concentration on the global scale and continuously in time. This observation can be provided only by using satellite instruments.

Up to now, the only measurement of the tropospheric CO concentration from space was made during the Measurement of Air Pollution from Satellites (MAPS) experiment with a first flight on November 12-14, 1981, and two flights in 1994 which occurred during April 9-19 and September 30 to October 14 [*Reichle et al.,* 1986, 1990; *Connors et al.,* 1996, 1999]. Several other observation programs of the troposphere are in progress or are scheduled for the forthcoming years. The Interferometric Monitor for Greenhouse Gases (IMG) instrument was launched aboard the Advanced Earth Observing System (ADEOS) platform in August 1996. The IMG instrument is designed to observe the distributions of greenhouse and other trace gases in the atmosphere: H_2O, CO_2, CH_4, N_2O, CO, and O_3. From its data, it is also possible to retrieve the vertical profile of atmospheric temperature [*Ogawa et al.,* 1994]. The Measurement of Pollution in the Troposphere (MOPITT), which uses the same gas correlation technique as MAPS, is scheduled for launch on the NASA EOS *Terra* spacecraft in summer 1999. MOPITT will measure both tropospheric CO profile and CO total column [*Drummond and Mand,* 1996; *Wang et al.,* 1999]. At the beginning of the next millennium, in 2003, the Infrared Atmospheric Sounding Interferometer (IASI) instrument will be launched aboard the European Meteorological Operational (METOP) platform to measure temperature and humidity and will also provide information on trace gases. The Tropospheric Emission Spectrometer (TES) is scheduled for launch on the NASA EOS CHEM spacecraft in 2003. TES will also measure tropospheric CO and CO total column [*Beer and Glavich,* 1989]. IMG, IASI, and TES all use Fourier transform spectroscopy to record, by nadir-viewing, the spectrum of the Earth-atmosphere system radiation in the thermal infrared spectral range from the top of the atmosphere.

Various inversion algorithms, based on fitting methods adapted from the one proposed by *Rodgers* [1976], are in development to retrieve vertical profiles of atmospheric temperature or concentrations of trace gases for nadir-looking instruments [*Clough et al.,* 1995; *Amato et al.,* 1996; *McMillan et al.,* 1997; *Pan et al.,* 1998; *Clerbaux et al.,* 1999]. In the framework of the IMG and IASI missions, we have started to develop a new inversion algorithm based on neural network techniques [*Clerbaux et al.,* 1995]. Neural networks offer a technical alternative to retrieve geophysical variables. Because of their adaptability, they can model a large range of physical functions [*Thiria et al.,* 1993]. Moreover, after the long preliminary learning phase, the inversion is very efficient during the operational phase. This feature is of particular interest in treating the important volume of data provided by the continuous measurements from space. During the last few years, the use of neural network techniques has increased in the atmospheric and oceanic fields. Among others, applications using neural networks have been described for cloud classification [*Lee et al.,* 1990; *Bankert,* 1994], retrieval of vertical atmospheric temperature profiles [*Escobar-Munoz et al.,* 1993; *Churnside et al.,* 1994; *Butler et al.,* 1996], radiative transfer modelization for climate studies [*Chevallier et al.,* 1998], and retrieval of oceanic surface winds [*Badran et al.,* 1991; *Thiria et al.,* 1993; *Stogryn et al.,* 1994]. *Chaboureau et al.* [1998] have developed an algorithm based on a neural network scheme to retrieve the vertical distribution of atmospheric water vapor and its total content, but, to our knowledge, these techniques have never been used before to retrieve CO atmospheric concentrations.

This paper describes a new neural network algorithm to retrieve the atmospheric CO total columns from the radiance spectra measured by the IMG instrument [*Clerbaux et al.,* 1995, 1998a]. After the description of the IMG instrument in section 2, we pose the geophysical problem and explain the forward and inverse problems in section 3. In section 4, some basic elements on the multilayer networks are provided. A detailed description of our inversion algorithm follows in section 5. In section 6, the performance of the inversion method on simulated data is presented along with the results of the retrieval of CO total columns on the global scale from the IMG spectra recorded between June 16 and 19, 1997.

2. IMG Instrument

The IMG instrument was launched on the Japanese ADEOS platform in August 1996. The satellite stopped sending information at the end of June 1997, providing about 9 months of data. The ADEOS platform had a Sun synchronous orbit and flew at an altitude of 800 km. A good global coverage of the Earth is obtained in 4 days. The IMG instrument was a Michelson interferometer which recorded the interferogram of the radiation of the Earth-atmosphere system. The spectrum was calculated by Fourier transform. The spectral resolution after apodization was 0.1 cm^{-1}, and the optical path difference was about 10 cm. The interferogram acquisition by the IMG instrument was organized in a cycle: it alternated series of six consecutive atmospheric measurements with phases of calibration with the onboard blackbody and with deep space [*Ogawa et al.,*

1994]. Each measurement took 10 s, during which the IMG instrument looked at a fixed point using an Image Motion Compensator (IMC) mirror, and the scanning mirror came back to its initial position in 3 s. For the calibration, the necessary time was 32 s. Between two consecutive atmospheric measurements, the satellite covered 86 km horizontally by projecting its orbit on the Earth surface, and between two series of six measurements, it covered about 297 km. This instrument used three detectors to cover the total spectral range from about 665 to about 3030 cm^{-1}: band 3 spread from 665 to 2000 cm^{-1}, band 2 spread from about 1875 to 2500 cm^{-1}, and band 1 spread from about 2190 to 3030 cm^{-1}. Each detector looked at a square of 8 km sides on the Earth surface. To retrieve the CO total columns, we work on the spectral range between 2000 and 2250 cm^{-1} (band 2), where the strong absorption lines of the CO 1-0 vibrational transition occur among absorption features associated with other constituents (H_2O, CO_2, O_3, N_2O) [*Clerbaux et al.*, 1998a]. Figure 1 illustrates a spectrum recorded in this spectral range by the IMG instrument at 60.138°E, 24.503°N on June 16, 1997.

3. Geophysical Problem

The satellites carrying nadir-viewing instruments like IMG or IASI have Sun synchronous orbits and fly at an altitude of about 800 km (in the forthcoming equation, we will note Z_m the altitude of the measure). In the spectral range between 2000 and 2250 cm^{-1} (4.44-5 μm), where we work to retrieve CO total columns, the solar contribution to the radiative budget of the Earth-atmosphere system is negligible with respect to the Earth's surface emission at the top of the atmosphere [*Lenoble*, 1993]. At the altitude of the measure, the radiance coming from the Earth-atmosphere system can be modeled by the radiative transfer equation, which can be written, in a simplified manner, for one spectral channel as

$$L_\nu(Z_m) = \varepsilon_\nu B(\nu, T_s)\,\tau_\nu(z_s, Z_m) + \int_{z_s}^{Z_m} B(\nu, T(z))\,\frac{\partial \tau_\nu(z, Z_m)}{\partial z}\,dz,$$

where $L_\nu(Z_m)$ is the radiance of the Earth-atmosphere system at the wave number ν observed at the altitude Z_m of the satellite, ε_ν is the Earth surface emissivity, $B(\nu, T)$ is the Planck function at the temperature T, $\tau_\nu(z, Z_m)$ is the atmospheric vertical transmittance between the measure height ($z = Z_m$) and the level z, and z_s and T_s are the altitude and the temperature of the Earth surface, respectively. The first part of this equation represents the contribution of the radiation emitted by the Earth surface; the second part is the atmospheric contribution. The weighting function, $[\partial \tau_\nu(z, Z_m)]/\partial z$, varies between 0 and 1 according to the importance of the contribution of each atmospheric layer to the total radiation at a given wave number. By using radiances measured at different spectral channels, we can reach different parts of the atmosphere in the inversion process. The data recorded by an instrument are the results of a complex function depending on different parameters: the emissivity of the Earth surface, the vertical profile of atmospheric temperature through the Planck function, the vertical profiles of atmospheric constituents, in particular, the water vapor which absorbs strongly in infrared, through the transmittance and the weighting function, and also the instrumental features (the noise and the instrumental function).

The solution of a data inversion problem consists in linking the studied physical variables with the measured quantities by a transfer function. The radiative transfer equation describes the forward problem. The inverse

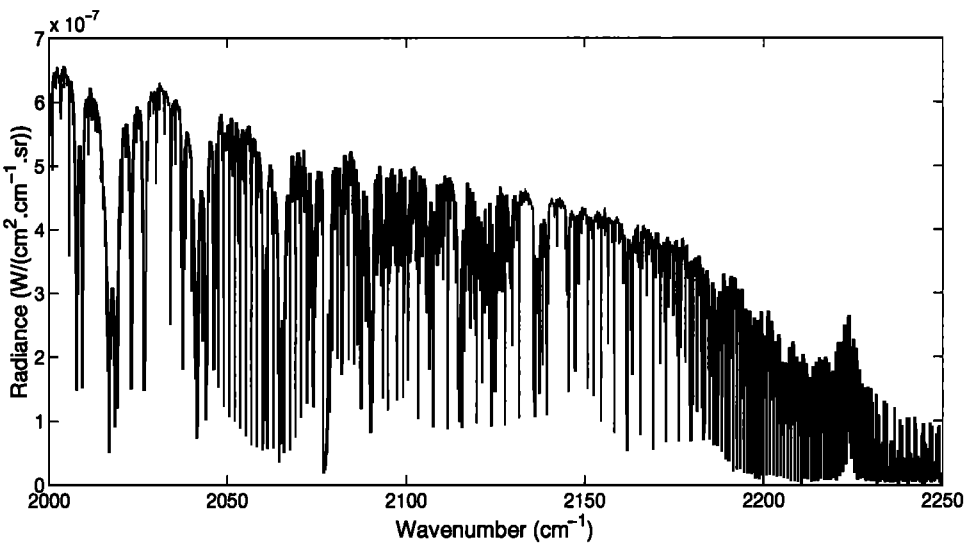

Figure 1. Radiance spectrum (W (cm^2 cm^{-1} sr)$^{-1}$), in the 2000-2250 cm^{-1} spectral range used for CO retrieval, recorded by the IMG instrument at 60.138°E, 24.503°N on June 16, 1997.

problem is the analytical inversion of this expression. It is ill-posed. Because of the strongly nonlinear behavior of the equation and the uncertainties on the measurements, there is more than one possible solution to this problem. Therefore we must find the best estimate of the function between the desired variables and the measurements. In classical methods, a priori information is used as criteria to determine the solution of the studied problem among all possible ones [*Rodgers,* 1976]. Neural network techniques allow the solution of regression problems by estimating a transfer function from a set of known situations which constitutes the a priori information necessary to solve the problem. *Blum and Li* [1991] prove that three-layer feed-forward perceptrons are "universal approximators" of functions and are then able to model a large range of physical phenomena. They demonstrate that any real multidimensional function, continuous on a compact subset or integrable on a measurable subset in $\mathbf{R}^n$, can be uniformly approximated by a three-layer feed-forward network, including two hidden layers of Heaviside function neurons and a linear output unit, with error less than ε, for any positive ε. This universality property can be extended for networks with hidden neurons with sigmoid transition functions. *Thiria et al.* [1993] have shown how neural networks can model a wide range of complex transfer functions. The authors provide a practical framework for the use of the neural networks to solve actual regression problems.

To develop a first version of our inversion algorithm based on neural networks, we assumed that we knew the instrumental function and the noise associated with the instrument. We started by fixing the Earth surface emissivity and the profiles of the other absorbing constituents. The three variables of our problem were then the measured spectra of radiance and the vertical profiles of atmospheric temperature and CO. We assumed that the temperature profiles associated with the spectra were provided. We then had to estimate the transfer function, allowing us to invert CO total columns from radiances measured at different wave numbers and temperatures measured at different vertical levels.

4. Multilayer Networks

In this work, a neural network is used to model a transfer function. This is a problem of multivariate nonlinear function approximation. This kind of problem is treated, in the literature, with multilayer networks, also called feed-forward networks. Before we describe our inversion algorithm, we will give some theoretical elements on the formal neuron, the neural network, and its development for a simple architecture as the one we have developed.

4.1. Neural Network Architecture

The formal neuron is the basic element of the network which calculates the desired function approximation. It is an elementary transfer function. Figure 2 presents a schematic diagram of a neuron. Its total input is the weighted sum A of the inputs x_i:

$$A = \sum_{i=1}^{n} w_i x_i = \mathbf{w} \cdot \mathbf{x},$$

where $\mathbf{w}$ is the vector of the weights w_i of the links reaching the neuron and $\mathbf{x}$ is the vector of the neuron inputs x_i. The weights measure the contributions of the neuron. The output y of the neuron, called its state, is a function of its total input:

$$y = y(\mathbf{w}, \mathbf{x}) = f(A).$$

The transition function f is chosen according to the problem that is to be solved.

A neural network is a set of neurons linked in a certain way depending on the network architecture. Figure 3 presents the diagram of a simple multilayer network. In this case, the neurons are organized in fully connected layers: a layer's units are not connected, but each of them is linked with all those of the next layer. In this way, signals are transmitted through the network from the first layer, called the input layer, which recopies the network inputs values, to the last layer, called the output layer, which provides, to the outside of the network, the results of the function approximation. Between the input and output layers, the network includes one or more layers, called hidden layers. The hidden layers realize, with the output one, the approximation calculations through the transmission process of each neuron as described previously. The network output $\mathbf{Y}$ is a function of the network inputs, which we gather together in a vector $\mathbf{x}$, and of the set of the weights, which we gather together in a matrix $\mathbf{W}$:

$$\mathbf{Y} = \mathbf{F}(\mathbf{W}, \mathbf{x}).$$

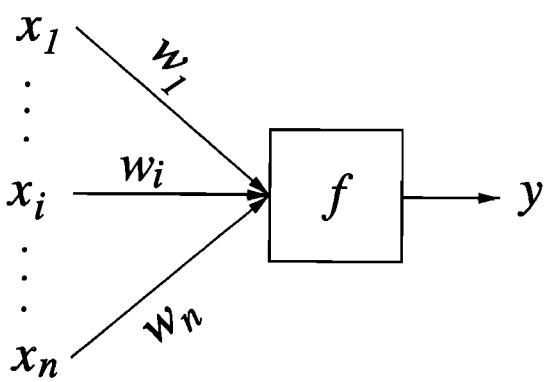

Figure 2. Diagram of a formal neuron. The inputs x_i reach the neuron through links associated with the weights w_i. The neuron state y is the result of the transition function f applied to the total input A, the weighted sum of the inputs x_i.

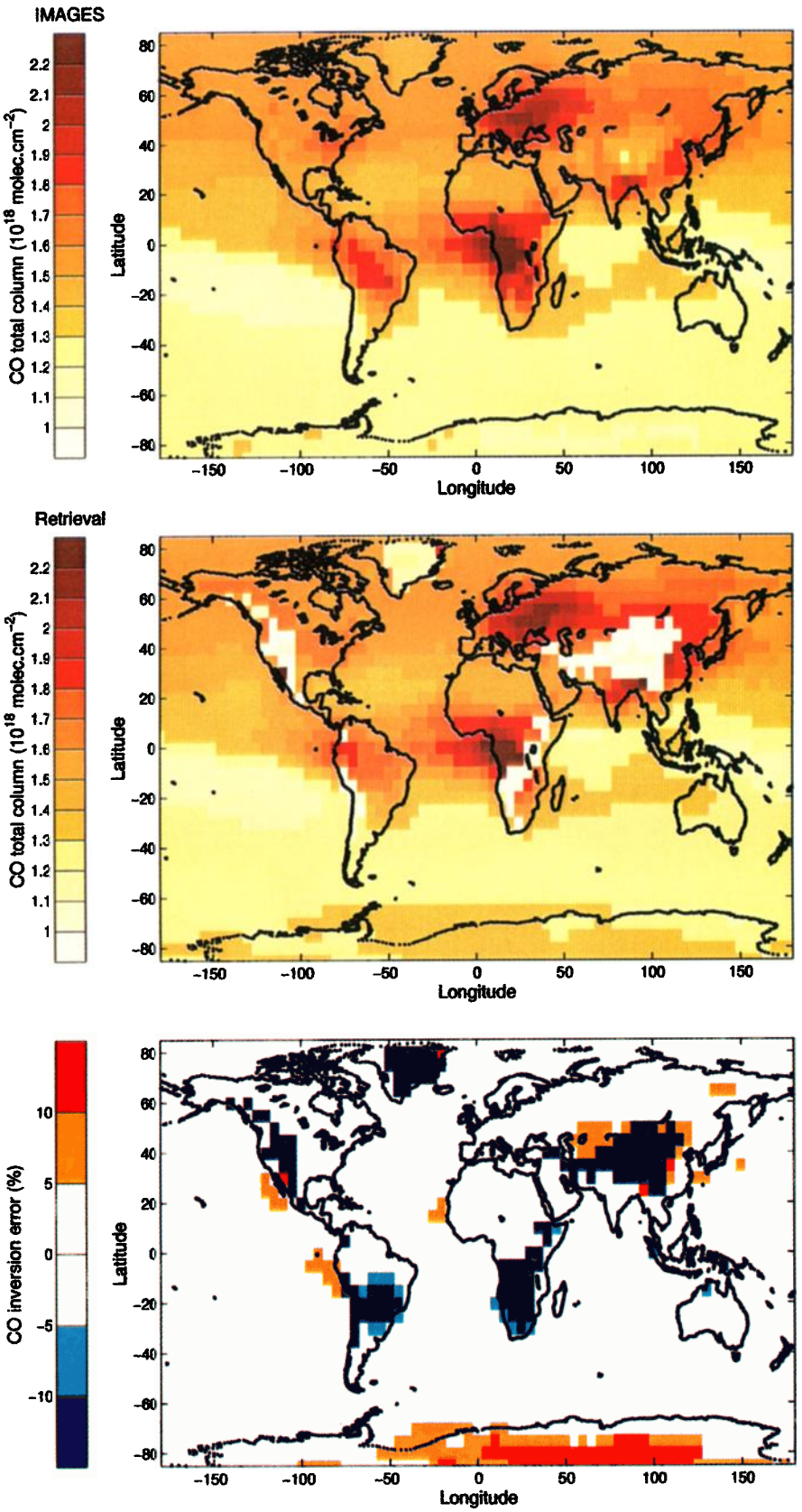

Plate 1. CO global distribution (total columns in molecules cm^{-2}) (top) as obtained by the IMAGES model for June and (middle) as retrieved by the network after simulation of Interferometric Monitor for Greenhouse Gases (IMG) measurements. (bottom) The relative differences (%) are also provided.

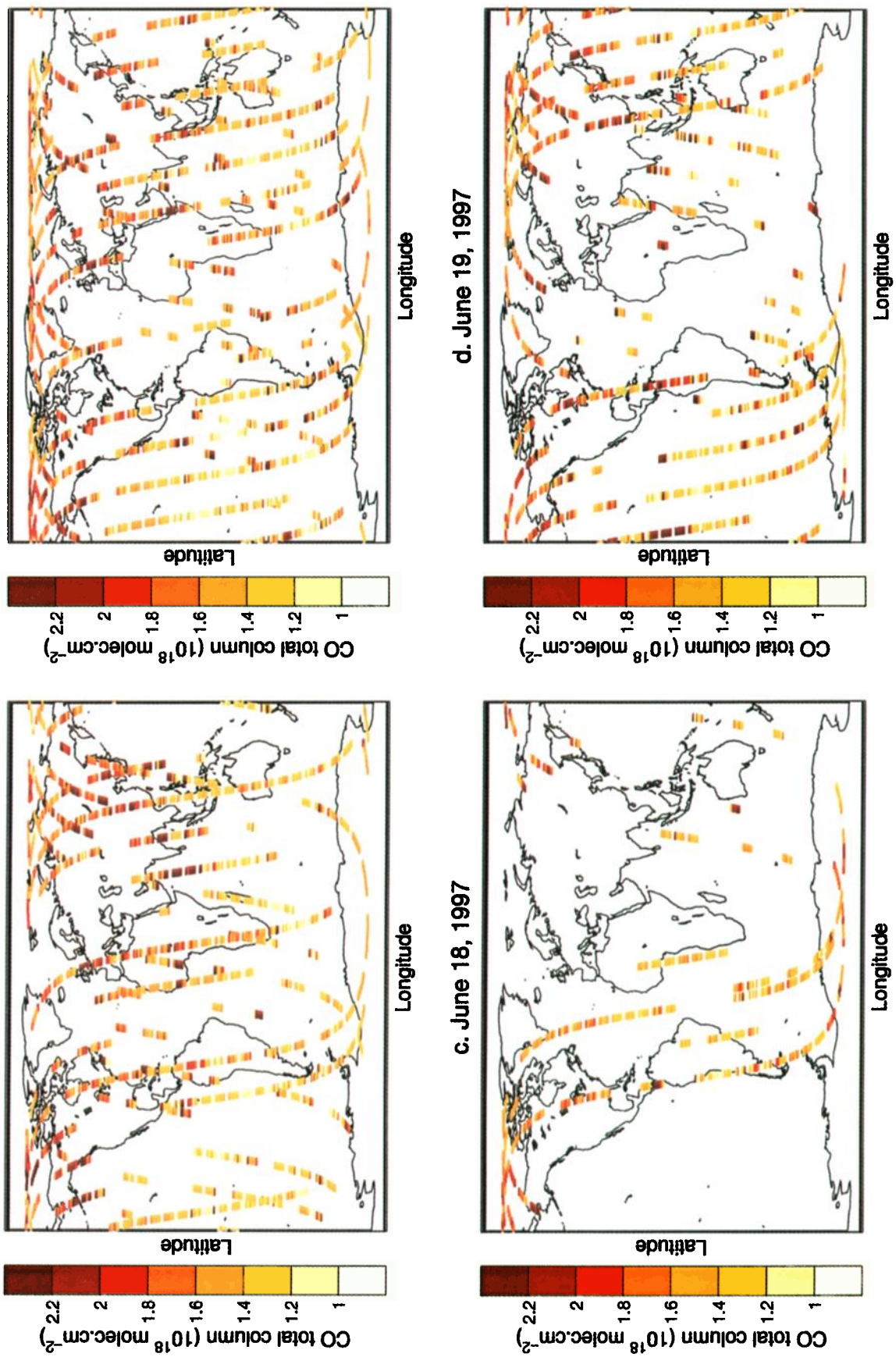

Plate 2. Results of the inversion of the data recorded by the IMG instrument the (a) 16th, (b) 17th, (c) 18th, and (d) 19th of June 1997. The colored bars correspond to the retrieved values of CO total column (molecules cm^{-2}) and represent the measured pixels enlarged to improve the legibility of the maps.

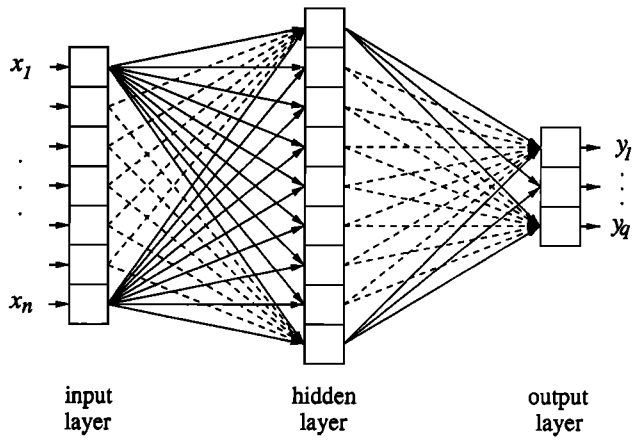

Figure 3. Diagram of a neural network composed of an input layer with n neurons, a hidden layer, and an output layer with q neurons.

To solve a particular problem, an adapted network architecture must be chosen. It consists in determining the number of network hidden layers, the number of units, their transition functions, and the topology of their connections. In the case of multilayer networks, the more commonly used transition functions are sigmoid ones, like $f(x) = 1/(1+e^{-x})$ or $f(x) = \tanh(x)$, for the hidden layers, the transition function of the output neurons being linear with $f(x) = x$. The definition of the architecture corresponds to the choice of a family of functions, $\mathbf{Y} = \mathbf{F}(\mathbf{W}, \mathbf{x})$, in which the best estimate of the studied function must be sought by fitting the weights' values in the learning phase [*Thiria et al.*, 1993]. The use of sigmoid functions as neuron transition functions gives to the algorithm its ability to model nonlinear phenomena. The number of neurons in the input and output layers is directly related to the physical problem being solved. The number of units in the hidden layers depends on the mathematical properties of the functions associated with the physics of the problem. It is determined carefully by using cross-validation methods [*Bishop*, 1995].

4.2. Network Learning Phase

To train the network, we need a database:

$$D = \{\mathbf{x}^n, \mathbf{d}^n\} \qquad n = 1, ..., N,$$

where $\mathbf{x}^n$ is a vector gathering together the inputs of the example n and $\mathbf{d}^n$ is the corresponding desired output. This database must include the information on the physics of the problem. The goal of the network training is to build a statistical model of the process which joins the inputs $\mathbf{x}^n$ with the desired outputs $\mathbf{d}^n$ by fitting the weights $\mathbf{W}$. The weights are calibrated to minimize a cost function $C(\mathbf{W})$:

$$C(\mathbf{W}) = \sum_{n=1}^{N} C^n(\mathbf{W}) = \sum_{n=1}^{N} ||\mathbf{d}^n - \mathbf{Y}^n||^2,$$

where $\mathbf{Y}^n = \mathbf{F}(\mathbf{W}, \mathbf{x}^n)$ is the output calculated by the network using $\mathbf{x}^n$. The database D is divided into three sets with no common elements. The first set, called the training (or learning) set, is used to minimize the cost function $C(\mathbf{W})$. The second one, called the validation set, allows selection of the suitable architecture and stopping of the training phase. The final performance is evaluated with the last set, called the test set. The learning set must be sufficiently large and statistically representative of all the situations which the network could meet to allow a successful generalization during the operational phase.

We use, in a sequential mode, the minimization method of the gradient descent with a back-propagation algorithm to calculate the gradient of the cost function in accordance with the weights. Further details on this minimization algorithm and on other training methods are given by *Bishop* [1995]. After the presentation of each element of the learning set, the network weights are modified according to

$$\mathbf{W}^t = \mathbf{W}^{t-1} - \eta \nabla C^t,$$

where $\mathbf{W}^t$ is the matrix collecting the weights modified at the end of the iteration t and η is the learning rate. To follow the training progress, after each presentation of the whole learning set, an error E is calculated for the validation set according to

$$E = \frac{1}{N_{\text{val}}} \sum_{n=1}^{N_{\text{val}}} ||\mathbf{d}^n - \mathbf{Y}^n||^2,$$

where N_{val} is the number of examples in the validation set. We apply the cross-validation method to determine the end of the learning phase [*Bishop*, 1995].

To find an efficient network, the training described previously is realized with different architectures, the best one being chosen by cross-validation using the test set and computing E. In theory, if the architecture is well chosen and if the network training is well achieved, the total transfer function modeled by the neural network is an accurate approximation of the conditional average of the output for each input. After the training phase, the weights of the network are fixed, and the operational phase can start. The learning phase is long because of the minimization process and the important number of weights to be determined. In the operational phase, the computations are faster because they are only simple algebraic operations.

5. CO Retrieval Algorithm

A multilayer neural network is used to find a function approximation to invert CO total columns from radiances measured at different wave numbers and temperatures at different levels. *Clerbaux et al.* [1998a] provided a selection of the relevant spectral channels to be used for CO inversion from IMG data. Among the intense CO absorption features, we have isolated those

for which the influence of other absorbing constituents is the weakest. This selection lowers the strong influence of the water vapor on the inversion results. There are 132 spectral channels satisfying this condition. We have chosen nine vertical levels, 0, 1, 3, 4, 5, 7, 10, 14, and 20 km, to represent the shape of the temperature profiles. The input layer includes 141 neurons, among which 132 are dedicated to radiances and nine are dedicated to temperatures. The network output, with a single neuron, provides the CO total column. In between, there are two hidden layers with five neurons each. The transition functions of the neurons are tanh functions for the hidden layers and a linear function for the output layer. We have used the neural network toolbox (version 2) of the MATLAB software (version 4) to develop our algorithm [*Demuth and Beale,* 1994].

We have seen that the development of a neural network requires a database. As there is a lack of measurements of CO on the global scale, we have chosen to work with simulated data. To provide realistic simulations of the IMG measurements, we have coupled a three-dimensional chemical-transport model with a line-by-line radiative transfer code as described by *Clerbaux et al.* [1998a]. The database includes, for different realistic geographical conditions, the radiances for the selected spectral channels, the temperatures at the nine vertical levels, and the corresponding CO total column value. The CO vertical profiles calculated by the Intermediate Model of the Annual and Global Evolution of Species (IMAGES) in the troposphere [*Müller and Brasseur,* 1995], and their colocated temperature profiles provided by the European Centre for Medium-Range Weather Forecasts (ECMWF), are used as inputs of the high-resolution Line-By-Line Radiative Transfer Model (LBLRTM) [*Clough et al.,* 1992; *Clough and Iacono,* 1995], adjusted to the IMG instrumental features (nadir view, optical path difference of 10 cm, satellite altitude of 800 km). The IMAGES model is driven by monthly averaged ECMWF fields of temperature, wind, and boundary conditions and provides the global distribution of chemical species on a $5° \times 5°$ horizontal resolution and on 25 vertical levels from the surface to an altitude of about 20 km. In this study, the monthly averaged distributions of CO calculated by IMAGES were used as inputs of the radiative transfer code. We started by assuming that the Earth behaved as a perfect blackbody (with an emissivity of 1) and that the instrumental function was an ideal $\sin(x)/x$. Mean atmospheric profiles of other absorbing constituents were set to the Air Force Geophysics Laboratory (AFGL) U.S. Standard Atmosphere 1976. Measurements were simulated for clear sky and aerosol-free conditions. As a first step, the network has been trained without considering the effect of the topography. In order to invert the IMG data recorded in June 1997, the IMG measurements were simulated for June, July, and August conditions. The noise of the IMG instrument, which is of the order of 2×10^{-9} W $(\text{cm}^2\ \text{cm}^{-1}\ \text{sr})^{-1}$ in the CO spectral range, was simulated by generating series of random numbers, uniformly distributed between -2×10^{-9} and 2×10^{-9}. This randomly simulated noise was added to the radiances coming from the radiative transfer model. In the database, we have collected the simulations with noise and the ones without noise. To complete the database, we have associated with each simulated measurement the corresponding ECMWF temperature profile and CO total column value. This latter was calculated from the IMAGES CO profile and its associated ECMWF temperature profile. The chemical-transport model used to simulate the measurements of the instrument must be chosen carefully. It must be as realistic as possible because the distribution retrieved by the network will be driven by the distribution provided by the model.

The simulation of the IMG measurements provided 9753 different cases composed of 132 corresponding radiances, nine temperature levels, and one CO total column. To select the elements of the training set, we added up the 132 radiances to reduce the dimensions of the problem. In the space formed by this sum and the temperature at ground level, we chose 6000 different cases representative of the dispersion of the sum of the radiances. After the composition of the learning set, the elements remaining in the database were included in the validation set. The test set was constituted with simulations with noise which had not been used in the learning set or in the validation one. For the three sets, the 141 network inputs were normalized between -1 and 1 to allow the use of sigmoid functions in the hidden layers. The learning, validation, and test sets include 6000, 3753, and 40,140 elements, respectively.

6. Results

We now describe the network operational phase. We show results of the algorithm on the test data set containing only simulations of IMG measurements never used for the network training phase or for the validation procedure. The network performance is checked with data which were not learned. The algorithm is then applied to invert real IMG measurements for four consecutive days of June 1997.

6.1. Inversion of Simulated Data

Each element of the test set has been presented to the network. The scatterplot for the 40,140 elements of the test set is provided in Figure 4. The cloud of points shows the comparison of the CO total columns calculated from the IMAGES profiles, which are the desired outputs, with the CO total columns retrieved by the network. If the inversion was perfect, all points would have been on the first bisector drawn in black. If a suitable network architecture is found, if the learning set is statistically representative, and if the learning phase is well achieved, the total transfer function of the network provides the conditional mean of the CO total column

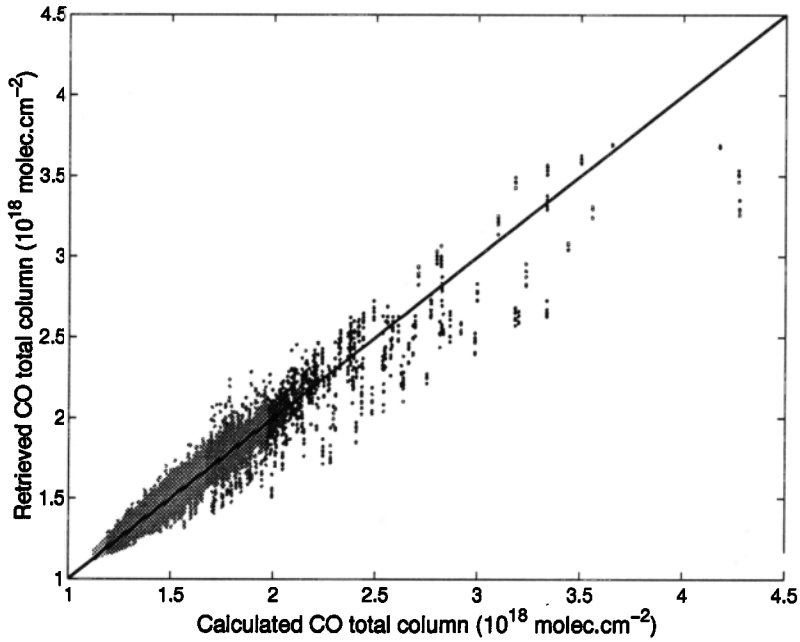

Figure 4. Scatterplot of the network for the test set. The cloud of points illustrates the comparison between the CO total columns (molecules cm^{-2}) calculated from the Intermediate Model of the Annual and Global Evolution of Species (IMAGES) model profiles and the CO total columns (molecules cm^{-2}) retrieved by the network. The first bisector is drawn in black. The gray scale highlights the four areas used to estimate the distribution of the inversion relative errors as a function of the CO total columns.

given the radiance spectrum and the temperature profile. For the middle values of CO total column, this approximation is well realized; the dots are well dispersed around the bisector. The performance decreases in the extreme limits, where the network has a tendency to overestimate the low CO total columns and to underestimate the high ones.

For each element of the test set, we have estimated a relative error between the CO total column calculated from the IMAGES profiles, the desired output, and the one retrieved by the network. This error is expressed as follows

$$e = \frac{d^k - Y^k}{d^k} \times 100$$

where d^k is the desired output of the example k of the test set and Y^k is the output calculated by the network from the example k input. We have checked the distribution of the results: for about 99% of the profiles, the absolute value of the error is less than 10%, and for more than 90%, it is less than 5%. As a 10% level of accuracy for CO retrieval was set as a requirement for the IASI mission [*Camy-Peyret and Eyre*, 1998], these results are quite satisfactory. The distribution of these inversion relative errors as a function of the CO total column is summarized in Table 1. We have divided the range of CO total column covered by the test set in four parts highlighted by the gray scale in Figure 4: low values (less than $1.19 \times 10^{+18}$ molecules cm^{-2}), "middle-low" values (between $1.19 \times 10^{+18}$ and $1.67 \times 10^{+18}$ molecules cm^{-2}), "middle-high" values (between $1.67 \times 10^{+18}$ and $1.97 \times 10^{+18}$ molecules cm^{-2}), and high values (higher than $1.97 \times 10^{+18}$ molecules cm^{-2}). The results presented are coherent with the observations on the scatterplot. For the low CO total columns, there is a small positive bias. For the middle values, the mean errors are close to 0. For the high values, there is a negative bias. The systematic error in the extreme limits can be attributed to the lack of low and high values of CO total column in the training set in comparison with the important number of middle values. The dispersion of the error increases with the CO total column. This results from the fact that the more the CO concentrations increase, the more particular CO profiles appear owing to strong CO emissions and redistribution by transport processes. These special events are probably not sufficiently represented in the training set.

Table 1. Distribution of Inversion Relative Errors as a Function of the CO Total Column

	Ranges of CO Total Column			
	Low	Middle Low	Middle High	High
Mean, %	1.32	0.20	0.18	-2.01
Standard deviation, %	1.21	2.72	4.30	7.45

Our algorithm is designed to invert data measured from space on the global scale. To check the network performance on a realistic case, we have studied the distribution of the calculated errors on the global scale. Plate 1 shows the CO total columns calculated for June conditions from the CO IMAGES profiles and the CO total columns retrieved by the neural network from the simulated spectra based on the same CO profiles. If we compare the two distributions, we note that the results provided by the algorithm well represent the distribution of CO total columns calculated from the IMAGES profiles except over relief areas. The relative error e between the two distributions is also shown in Plate 1. On most parts of the world, the inversion error is less than 5% in absolute value. These results are coherent with those achieved on the test set. In each case where the error was found to exceed 5%, we studied in detail why the network failed to retrieve CO properly. As the topography was not considered during the training phase, important errors are found over the Himalaya, Greenland, the Andes, the Rocky Mountains, South Africa, and New Guinea island, where the algorithm underestimates CO total columns, and over Antarctica, where it overestimates them. In the vicinity of Greenland, the Rocky Mountains, and the Himalaya, there are isolated points where the error is higher than 10% (red points) close to errors of -10% (dark blue points). This feature results from the vertical interpolation required to change the σ pressure scale of the IMAGES model into a regular 1 km altitude grid needed for radiative calculations. In South America and South Africa, close to the relief areas, we find errors lower than -5% which correspond to emissions of CO by biomass burning. In these cases, the CO profiles present important CO concentrations in the boundary layer which are difficult to detect with instruments like IMG, as reported by *Clerbaux et al.* [1998a]. This is also the case over Australia and Sumatra, in two specific locations. The errors between 5 and 10% near the Rocky Mountains, the Andes, the Sahara desert, Siberia, and Japan in the Pacific Ocean result from the transport of the emitted CO which is associated with profiles whose shapes are very peculiar in IMAGES. Around the Himalaya, errors between 5 and 10% are due to emission profiles which are different from those met in South America and South Africa. An increase of the number of all these particular cases in the training set would probably improve the quality of the results.

This comparison with the chemical-transport model IMAGES could probably be improved by the calculation of the averaging kernels associated with IMG, as the instrument is not equally sensitive to the different atmospheric layers [*Pougatchev et al.*, 1995, 1998]. This will be implemented for the next version of the algorithm in order to efficiently compare our retrieval results with those of other inversion methods and with other atmospheric measurements.

6.2. Inversion of IMG Data

Very preliminary results of CO inversion using IMG data were presented by *Clerbaux et al.* [1999]. Here we have applied the algorithm to retrieve CO total columns from the data recorded by the IMG instrument between June 16 and 19, 1997. The inputs of the network were the selected spectral channels [*Clerbaux et al.*, 1998a] for the IMG spectra (IMG data Level 1C) and the nine levels of atmospheric temperature for retrieved profiles (IMG data Level 2). To check the rapidity of our algorithm, we have estimated the time necessary to retrieve CO total columns from the IMG data available for June 17, 1997 (318 series of six measurements). This global inversion took less than 3 min of CPU time on a DEC Alpha workstation.

The results of the inversion for the four consecutive days are presented in Plate 2. As expected, the higher columns appear in the Northern Hemisphere in polluted regions, and lower values are retrieved in the Southern Hemisphere. To illustrate this feature, we have isolated a succession of series of measurements along one orbit from 151.091°E, 73.062°S to 48.146°E, 80.359°N and crossing the equator at a longitude of about 116°E. The retrieved CO total column is shown in Figure 5 (solid line) against latitude (both averaged on six successive measurements) and compared to the IMAGES simulations for June at a longitude of 116°E (dashed line). To extend the comparison, we have also drawn the latitudinal variation of the Model for Ozone and Related Chemical Tracers (MOZART) simulations [*Brasseur et al.*, 1998; *Hauglustaine et al.*, 1998] for June 16 at a longitude of 116°E (dashed-dotted line). MOZART is a global chemical-transport model driven by dynamical and physical fields precalculated by a general circulation model (GCM) and provided every 3 hours. MOZART simulates the distribution of chemical species in the troposphere with a time step of 20 min. The horizontal resolution of this model is about 2.8° in both longitude and latitude, and it extends from the surface to an altitude of about 35 km with 25 vertical levels. The amplitude of the latitudinal variation in IMAGES is weaker than the one in MOZART. This feature is mainly associated with different transport schemes and dynamical fields used in the two models. An intercomparison of the CO distributions provided by current tropospheric models is discussed by *Kanakidou et al.* [1999] (part of a special issue on CO). In the Northern Hemisphere, the distribution of the inversion results is between those of the models. In the Southern Hemisphere, the CO total columns retrieved by the network are higher than the values provided by the two models. This could result from the fact that the two models are driven by dynamical fields representative of a mean climatological state rather than actual meteorological conditions prevailing during the measurement period.

By checking the results shown in Plate 2 in more detail, we note some anomalies. In some cases, wrong

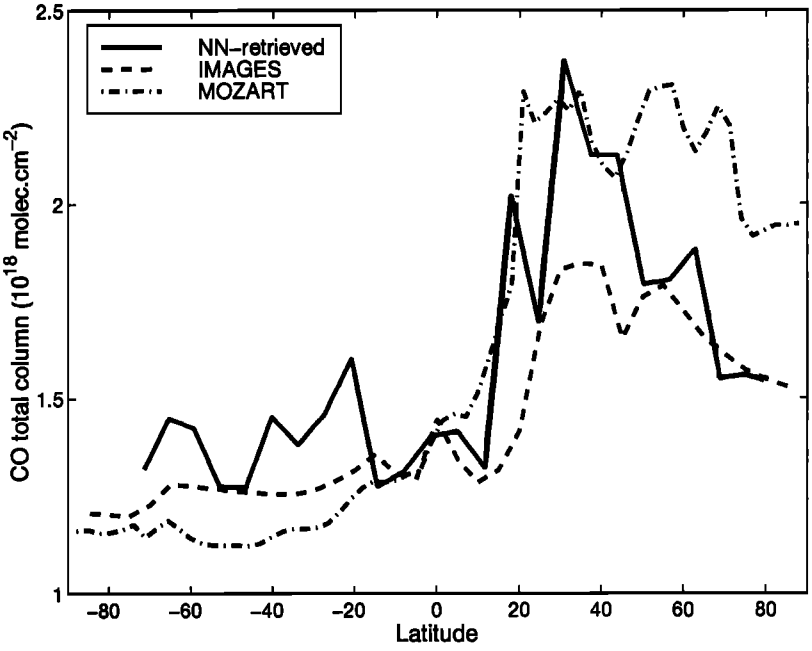

Figure 5. Latitudinal variations of the CO total columns (molecules cm^{-2}) as retrieved by the network for June 16, 1997 (solid line), as calculated from the IMAGES simulations for June (dashed line) and as calculated from the Model for Ozone and Related Chemical Tracers (MOZART) simulations for June 16 (dashed-dotted line) for a longitude of 116°E at the equator.

interferograms result in poor quality spectra. They are very distorted and present too low intensities. They are outside of the range covered by the learning database, the sigmoid transfer functions of the neurons are saturated, and the network provides very high values of CO total column. A second source of error comes from the fact that neither clouds nor aerosols were considered during the learning phase. In these cases, the signal is more or less attenuated according to the cloud covering. Plate 3 presents an example of measurements recorded by IMG on June 16, 1997. The spectra were recorded every 86 km between 60.900°E, 21.433°N and 60.138°E, 24.503°N. The attenuation of the signal increases from the first spectrum to the second one and decreases from the second spectrum to the fifth one. So, we can note that the measure was little disturbed by the presence of clouds during the acquisition of the first interferogram and more affected during the acquisition of the second and third interferograms. In the case of the presence of clouds, sensitivity studies are in progress to estimate their impact on the inversion results. As complementary information on the cloud covering is not provided with the IMG spectra, a detailed study of the impact of the clouds on the radiances recorded between 2000 and 2250 cm^{-1} will be undertaken.

7. Conclusions and Discussion

In order to treat the measurements provided by the new generation of remote sensors recording the radiance of the Earth-atmosphere system by nadir-viewing using Fourier transform spectrometry, we have developed a new inversion algorithm based on neural networks. This method allows to work with radiances associated with different wave numbers simultaneously and consequently lowers interfering contributions of instrumental noise and other absorbing species, in particular, the water vapor. Using a first version of the algorithm, we have checked its performance against simulated data. These first results are quite satisfying with regard to the expected errors after the preliminary sensitivity studies. This first version has been applied to the data recorded by the IMG instrument during four consecutive days in June 1997 to retrieve CO total columns. This algorithm has proved its efficiency in retrieving realistic CO values in a short amount of time, which would allow to its use for operational CO inversion. We have started to compare the performance of this new algorithm with algorithms currently developed for other instruments, using a common data set [*Clerbaux et al.*, 1998b]. The results of this study will be provided in a forthcoming paper.

Improvements will be brought to this algorithm to increase its performance on some specific cases (clouds, topography, biomass burning, and highly polluted regions) identified in this study. We plan to train the network using a realistic topography. A preliminary sorting of the spectra, before the inversion, will allow separate treatment of the measurements too much affected by the presence of clouds and the elimination of

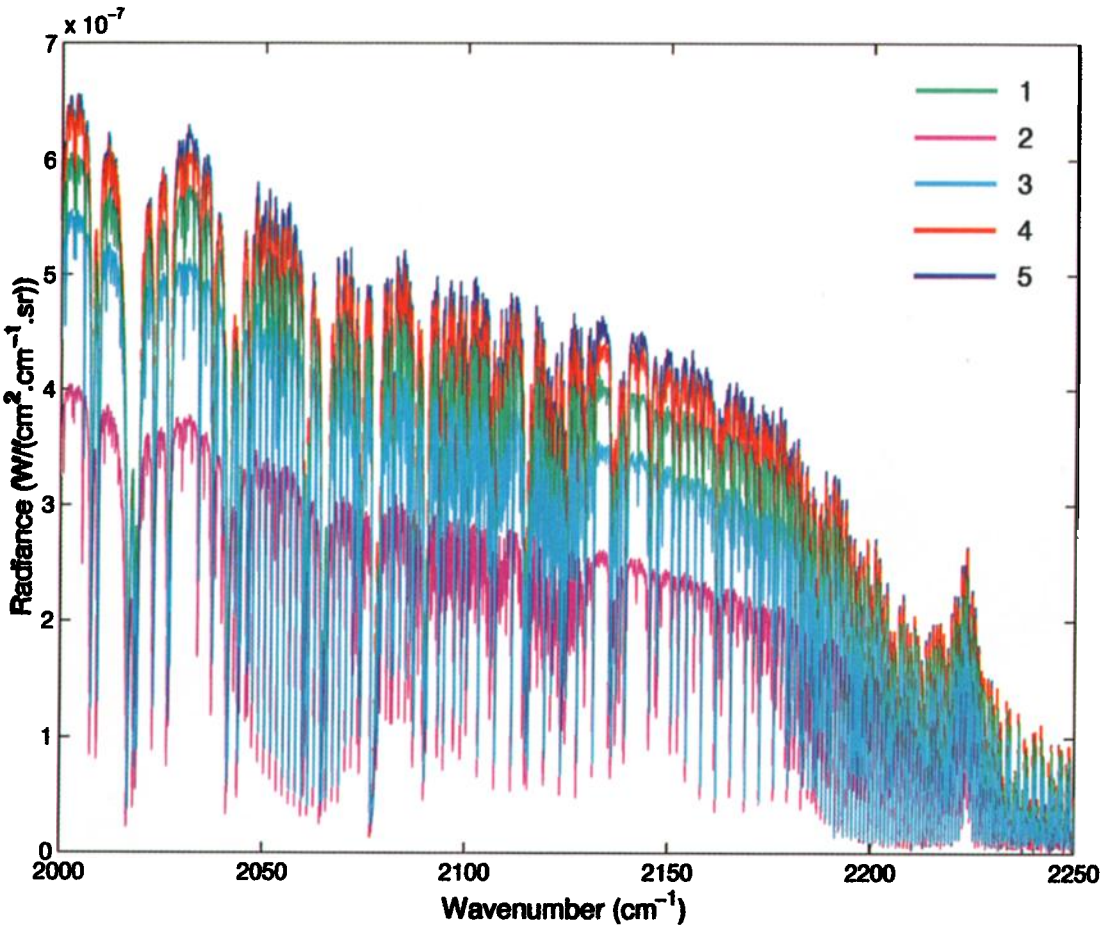

Plate 3. Succession of six radiance spectra (W $(cm^2\ cm^{-1}\ sr)^{-1}$), in the 2000-2250 cm^{-1} spectral interval, recorded by the IMG instrument between 60.900°E, 21.433°N and 60.138°E, 24.503°N on June 16, 1997. The three first spectra are attenuated in comparison with the two last ones. On the satellite orbit, the interferogram acquisition was perturbed by the presence of clouds.

those corresponding to wrong interferograms. To improve the results of the algorithm on specific high and low CO abundances, we will replace, for the development phase, the results of the IMAGES model (about 2500 profiles per month) with the results of the newly developed MOZART model. By using CO global distributions of MOZART averaged on each day, we will obtain about $8192 \times 30 = 245,760$ profiles per month. Furthermore, available ground-based and airborne measured CO profiles could be added to the database to take into account real vertical variability of atmospheric profiles in the development of the algorithm. This increase of the realistic cases in the CO data base will allow us to improve the training of the network. In spite of the problems highlighted in this study, the retrieval of the CO total columns from high-resolution nadir radiances seems to be workable by using an algorithm based on the neural network techniques.

Acknowledgments. We acknowledge Patrick Chazette (LSCE) for helpful discussions and Carlos Mejia (LODYC) for his help in the field of neural networks. The authors thank IMGDIS/ERSDAC for providing the IMG data. We are grateful to Cathy Boonne (Institut Pierre-Simon Laplace) for extracting the data and to Jean-François Müller (Belgian Institute for Space Aeronomy) and Didier Hauglustaine (Service d'Aéronomie du CNRS) for providing the outputs of the IMAGES and MOZART models. The present study was supported by the EC program NEUROSAT (ENV4-CT96-0314) and was undertaken in the framework of the ISSWG (IASI Sounding Science Working Group) activities under the auspices of EUMETSAT (European Organisation for the Exploitation of Meteorological Satellites) and CNES (Centre National d'Etudes Spatiales).

References

Amato, U., I. De Feis, and C. Serio, Linearization pseudo-noise and its effect on the retrieval of atmospheric state from infrared spectral radiances, *Geophys. Res. Lett.*, *23*(18), 2565-2568, 1996.

Badran, F., S. Thiria, and M. Crepon, Wind ambiguity removal by the use of neural network techniques, *J. Geophys. Res.*, *96*(C11), 20,521-20,529, 1991.

Bankert, R. L., Cloud classification of AVHRR imagery in maritime regions using a probabilistic neural network, *J. Appl. Meteorol.*, *33*, 909-918, 1994.

Beer, R., and T. A. Glavich, Remote sensing of the troposphere by infrared emission spectroscopy, *Proc. SPIE Int. Soc. Opt. Eng., 1129*, 42-48, 1989.

Bishop, C. M., *Neural Networks for Pattern Recognition*, 482 pp., Oxford Univ. Press, New York, 1995.

Blum, E., and L. Li, Approximation theory and feedforward networks, *Neural Networks, 4*, 511-515, 1991.

Brasseur, G. P., D. A. Hauglustaine, S. Walters, P. J. Rasch, J.-F. Müller, C. Granier, and X. X. Tie, MOZART, a global chemical transport model for ozone and related chemical tracers, 1, Model description, *J. Geophys. Res., 103*(D21), 28,265-28,289, 1998.

Butler, C. T., R. v. Z. Meredith, and A. P. Stogryn, Retrieving atmospheric temperature parameters from DMSP SSM/T-1 data with a neural network, *J. Geophys. Res., 101*(D3), 7075-7083, 1996.

Camy-Peyret, C., and J. Eyre, IASI science plan, A report from the IASI Sounding Science Working Group, Eumetsat, Germany, 1998.

Chaboureau, J.-P., A. Chédin, and N. A. Scott, Remote sensing of the vertical distribution of atmospheric water vapor from the TOVS observations: Method and validation, *J. Geophys. Res., 103*(D8), 8743-8752, 1998.

Chevallier, F., F. Chéruy, N. A. Scott, and A. Chédin, A neural network approach for a fast and accurate computation of a longwave radiative budget, *J. Appl. Meteorol., 37*(11), 1385-1397, 1998.

Churnside, J. H., T. A. Stermitz, and J. A. Schroeder, Temperature profiling with neural network inversion of microwave radiometer data, *J. Atmos. Oceanic Technol., 11*(1), 105-109, 1994.

Clerbaux, C., P. Chazette, and G. Mégie, Tropospheric concentrations of infrared absorbing molecules using a nadir-looking Fourier transform spectrometer: Passive infrared remote sensing of clouds and the atmosphere, III, *Proc. SPIE Int. Soc. Opt. Eng., 2578*, 148-153, 1995.

Clerbaux, C., P. Chazette, J. Hadji-Lazaro, G. Mégie, J.-F. Müller, and S. A. Clough, Remote sensing of CO, CH_4, and O_3 using a spaceborne nadir-viewing interferometer, *J. Geophys. Res., 103*(D15), 18,999-19,013, 1998a.

Clerbaux, C., J. Hadji-Lazaro, S. Payan, C. Camy-Peyret, and J. Wang, Intercomparison of inversion algorithms for the retrieval of CO from IMG/IASI spectra, paper presented at 8th International Workshop on Atmospheric Science from Space Using Fourier Transform Spectrometry (ASSFTS), CNES-Météo-France-CNRS-INSU, Toulouse, 1998b.

Clerbaux, C., J. Hadji-Lazaro, S. Payan, C. Camy-Peyret, and G. Mégie, Retrieval of CO columns from IMG/ADEOS spectra, *IEEE Trans. Geosci. Remote Sens., 37*(3), 1657-1661, 1999.

Clough, S. A., and M. J. Iacono, Line-by-line calculations of atmospheric fluxes and cooling rates, 2, Application to carbon dioxide, ozone, methane, nitrous oxide and the halocarbons, *J. Geophys. Res., 100*(D8), 16,519-16,535, 1995.

Clough, S. A., M. J. Iacono, and J.-L. Moncet, Line-by-line calculations of atmospheric fluxes and cooling rates: application to water vapor, *J. Geophys. Res., 97*(D14), 15,761-15,785, 1992.

Clough, S. A., C. P. Rinsland, and P. D. Brown, Retrieval of tropospheric ozone from simulations of nadir spectral radiances as observed from space, *J. Geophys. Res., 100*(D8), 16,579-16,593, 1995.

Connors, V. S., M. Flood, T. Jones, B. Gormsen, S. Nolf, and H. G. Reichle Jr., Global distribution of biomass burning and carbon monoxide in the middle troposphere during early April and October 1994, in *Biomass Burning and Global Change*, edited by J. S. Levine, pp. 99-106, MIT Press, Cambridge, Mass., 1996.

Connors, V. S., B. B. Gormsen, S. Nolf, and H. G. Reichle Jr., Spaceborne observations of the global distribution of carbon monoxide in the middle troposphere during April and October 1994, *J. Geophys. Res.*, in press, 1999.

Crutzen, P. J., and P. H. Zimmermann, The changing photochemistry of the troposphere, *Tellus, 43AB*, 136-151, 1991.

Demuth, H., and M. Beale, *Neural Network Toolbox for Use With MATLAB, User's Guide, Version 2*, The MathWorks Inc., Natick, Mass., 1994.

Drummond, J. R., and G. S. Mand, The measurement of pollution in the troposphere (MOPITT) instrument: Overall performances and calibration requirements, *J. Atmos. Oceanic Technol., 13*, 314-320, 1996.

Escobar-Munoz, J., A. Chedin, F. Cheruy, and N. Scott, Réseaux de neurones multi-couches pour la restitution de variables thermodynamiques atmosphériques à l'aide de sondeurs verticaux satellitaires, *C. R. Acad. Sci., Ser. II, 317*, 911-918, 1993.

Hauglustaine, D. A., G. P. Brasseur, S. Walters, P. J. Rasch, J.-F. Müller, L. K. Emmons, and M. A. Carroll, MOZART, a global chemical transport model for ozone and related chemical tracers, 2, Model results and evaluation, *J. Geophys. Res., 103*(D21), 28,291-28,335, 1998.

Kanakidou, M., et al., 3-D global simulations of tropospheric CO distributions - Results of the GIM/IGAC intercomparison 1997 exercise, *Chemosphere*, in press, 1999.

Lee, J., R. C. Weger, S. K. Sengupta, and R. M. Welch, A neural network approach to cloud classification, *IEEE Trans. Geosci. Remote Sens., 26*, 846-855, 1990.

Lenoble, J., *Atmospheric Radiative Transfer*, 532 pp., A. Deepak, Hampton, Va., 1993.

Logan, J. A., M. J. Prather, S. C. Wofsy, and M. B. McElroy, Tropospheric chemistry: A global perspective, *J. Geophys. Res., 86*(C8), 7210-7254, 1981.

McMillan, W. W., L. L. Strow, W. L. Smith, H. E. Revercomb, H. L. Huang, A. M. Thompson, D. P. McNamara, and W. F. Ryan, Remote sensing of carbon monoxide over the continental United States on September 12-13, 1993, *J. Geophys. Res., 102*(D9), 10,695-10,709, 1997.

Müller, J.-F., and G. Brasseur, IMAGES: A three-dimensional chemical transport model of the global troposphere, *J. Geophys. Res., 100*(D8), 16,445-16,490, 1995.

Novelli, P. C., K. A. Masarie, and P. M. Lang, Distributions and recent changes of carbon monoxide in the lower troposphere, *J. Geophys. Res., 103*(D15), 19,015-19,033, 1998.

Ogawa, T., H. Shimoda, M. Hayashi, R. Imasu, A. Ono, S. Nishinomiya, and H. Kobayashi, IMG: Interferometric measurement of greenhouse gases from space, *Adv. Space Res., 14*(1), 25-28, 1994.

Pan, L., J. C. Gille, D. P. Edwards, P. L. Bailey, and C. D. Rodgers, Retrieval of tropospheric carbon monoxide for the MOPITT experiment, *J. Geophys. Res., 103*(D24), 32,277-32,290, 1998.

Pougatchev, N. S., B. J. Connor, and C. P. Rinsland, Infrared measurements of the ozone vertical distribution above Kitt Peak, *J. Geophys. Res., 100*(D8), 16,689-16,697, 1995.

Pougatchev, et al., Ground-based infrared solar spectroscopic measurements of carbon monoxide during 1994 measurement of air pollution from space flights, *J. Geophys. Res., 103*(D15), 19,317-19,325, 1998.

Reichle, H. G., Jr., V. S. Connors, J. A. Holland, W. D. Hypes, H. A. Wallio, J. C. Casas, B. B. Gormsen, M. S. Saylor, and W. D. Hesketh, Middle and upper tropospheric carbon monoxide mixing ratios as measured by a satellite-borne remote sensor during November 1981, *J. Geophys. Res., 91*(D10), 10,865-10,887, 1986.

Reichle, H. G., Jr., V. S. Connors, J. A. Holland, R. T. Sherrill, H. A. Wallio, J. C. Casas, E. P. Condon, B. B. Gormsen, and W. Seiler, The distribution of middle tropospheric carbon monoxide during early October 1984, *J. Geophys. Res., 95*(D7), 9845-9856, 1990.

Rodgers, C. D., Retrieval of atmospheric temperature and composition from remote measurements of thermal radiation, *Rev. Geophys., 14*(4), 609-624, 1976.

Stogryn, A. P., C. T. Butler, and T. J. Bartolac, Ocean surface wind retrievals from special sensor microwave imager data with neural networks, *J. Geophys. Res., 99*(C1), 981-984, 1994.

Thiria, S., C. Mejia, F. Badran, and M. Crepon, A neural network approach for modeling nonlinear transfer functions: Application for wind retrieval from spaceborne scatterometer data, *J. Geophys. Res., 98*(C12), 22,827-22,841, 1993.

Wang, J., J. C. Gille, P. L. Bailey, J. R. Drummond, and L. Pan, Instrument sensitivity and error analysis for the remote sensing of tropospheric carbon monoxide by MOPITT, *J. Atmos. Oceanic Technol., 16,* 465-474, 1999.

World Meteorological Organization (WMO), Scientific assessment of ozone depletion: 1994, *Global Ozone Res. Monit. Pro. Rep. 37,* Geneva, 1995.

C. Clerbaux and J. Hadji-Lazaro, Service d'Aéronomie du CNRS, Université Paris 6, 4, place Jussieu, BP 102, 75252 Paris Cedex 05, France. (jha@aero.jussieu.fr)

S. Thiria, LODYC, Université Paris 6, 4, place Jussieu, BP 100, 75252 Paris Cedex 05, France.

(Received April 2, 1999; revised June 15, 1999; accepted June 17, 1999.)